nature astronomy

LETTERS

https://doi.org/10.1038/s41550-020-01263-2

Check for updates

# The origin of reconnection-mediated transient brightenings in the solar transition region

Shah Mohammad Bahauddin[1]✉, Stephen J. Bradshaw[2] and Amy R. Winebarger[3]

**The ultraviolet emission from the solar transition region is dominated by dynamic, low-lying magnetic loops. The enhanced spatial and temporal resolution of the solar observation satellite Interface Region Imaging Spectrograph (IRIS) has made it possible to study these structures in fine detail. IRIS has observed 'transient brightenings' in these loops, associated with strong excess line broadenings[1,2] providing important clues to the mechanisms that heat the solar atmosphere. However, the physical origin of the brightenings is debated. The line broadenings have been variously interpreted as signatures of nanoflares[3], magneto-hydrodynamic turbulence[4], plasmoid instabilities[5] and magneto-acoustic shocks[6]. Here we use IRIS slit-jaw images and spectral data, and the Atmospheric Imaging Assembly of the Solar Dynamics Observatory spacecraft, to show that the brightenings are consistent with magnetic-reconnection-mediated impulsive heating at field-line braiding sites in multi-stranded transition-region loops. The spectroscopic observations present evidence for preferential heating of heavy ions from the transition region and we show that this is consistent with ion cyclotron turbulence caused by strong currents at the reconnection sites. Time-dependent differential emission measure distributions are used to determine the heating frequency[7–9] and to identify pockets of faintly emitting 'super-hot' plasma. The observations we present and the techniques we demonstrate open up a new avenue of diagnostics for reconnection-mediated energy release in solar plasma.**

IRIS has observed small-scale (a few million metres, Mm) loop-like structures with intermittent brightenings in the Sun's active regions, which are associated with excess line broadenings[1,2]. These rapidly evolving brightenings are remarkably consistent with previous High-Resolution Coronal Imager (Hi-C) observations of reconnection-mediated heating in coronal loops[10]. Figure 1 (and Supplementary Fig. 1) shows information revealed by IRIS regarding the geometries and the evolution of the brightened loops. Although Atmospheric Imaging Assembly (AIA) images and Helioseismic and Magnetic Imager (HMI) magnetograms from the Solar Dynamics Observatory (SDO) present these loops as singular, monolithic structures, having opposite polarity at their foot-points, unsharp masking applied to IRIS 1,400 Å slit-jaw images demonstrates the existence of substructures within the brightening regions, which we interpret to mean that the loops are multi-stranded. The 131 Å and 94 Å SDO/AIA passbands detect a signature of the aftermath of heating at the braiding sites: 'super-hot' plasma. The observations presented in Figs. 2 and 3 show a pixel-by-pixel analysis of the brightenings labelled 1 and 3 in Fig. 1, and the evolution of their spectra. The IRIS 1,400 Å channel is the primary mode for this analysis owing to its fast cadence and high spatial resolution, and because it contains several lines readily available for plasma diagnostics. The intensity of Si IV 1,403 Å emission varies strongly on the 50–100-s timescales over which the loops in Figs. 2 and 3 were rastered. This implies the presence of even faster variations below the timescale limit imposed by the rastering process. The density-sensitive O IV line ratio (1,399.766 Å/1,401.157 Å, Supplementary Table 1) finds number densities of $10^{11}$ cm$^{-3}$ in the brightenings and densities of $10^{13}$ cm$^{-3}$ in the darker regions, which are more characteristic of the upper chromosphere (Extended Data Fig. 1).

The Si IV 1,403 Å line changes profoundly in the bright regions; it becomes multi-peaked (Fig. 1, lower panel) and broadens substantially (full-width at half-maximum $\Delta\lambda \approx 300$ km s$^{-1}$). We decomposed the Si IV 1,403 Å profiles into two Gaussian components and found strong bi-directional flows with a maximum speed of 100 km s$^{-1}$ towards and away from the observer. The two components of the bi-directional flows feature non-thermal components as large as 100 km s$^{-1}$ (Figs. 2 and 3, see panels for Si IV(a) for the blue-shifted component and Si IV(b) for the red-shifted component). Strong Doppler shifts with broad non-thermal components are also observed in the S IV 1,404 Å line profile. The downwards (surfacewards) flow observed in Si IV 1,403 Å is somewhat slower than the upwards flow to conserve momentum, since the atmosphere is gravitationally stratified. However, the O IV 1,401 Å line profile is only ever weakly red-shifted (maximum 25 km s$^{-1}$) with a single component and no non-thermal broadening is observed.

We conjecture that the explanation for these different line profiles may lie in the formation temperatures of Si IV ($10^{4.8}$ K) and O IV ($10^5$ K). The bi-directional jet material cools as it expands and so a stronger signature of the flow is observed in the lower-temperature line; if the emission from O IV emanates from the slower, inner (and thus warmer) region of the reconnection jet, the Doppler-shifted components may not be sufficiently separable to resolve. Spectroscopic observations across a broader range of line formation temperatures than are currently available, and/or modelling and predictions of line profiles in non-equilibrium conditions for strong outflows, should address this matter in detail.

To further investigate the differences between the heavier (silicon and sulfur) ions, and lighter (oxygen) ion and their underlying causes, the ratio of the peak Si IV 1,403 Å and O IV 1,401 Å intensities is plotted for each pixel in Figs. 2 and 3 (top-right panels). This ratio is a strong diagnostic for non-equilibrium ionization and models show that enhanced values are induced by impulsive heating when density-dependent dielectronic recombination is included in the line-formation process and ions with enhanced lifetimes are transported into denser layers of the atmosphere[11]. Large Si/O peak

[1]Laboratory of Atmospheric and Space Physics, University of Colorado Boulder, Boulder, CO, USA. [2]Department of Physics and Astronomy, Rice University, Houston, TX, USA. [3]Heliophysics and Planetary Science Office, NASA Marshall Space Flight Center, Huntsville, AL, USA. ✉e-mail: shahmohammad.bahauddin@colorado.edu

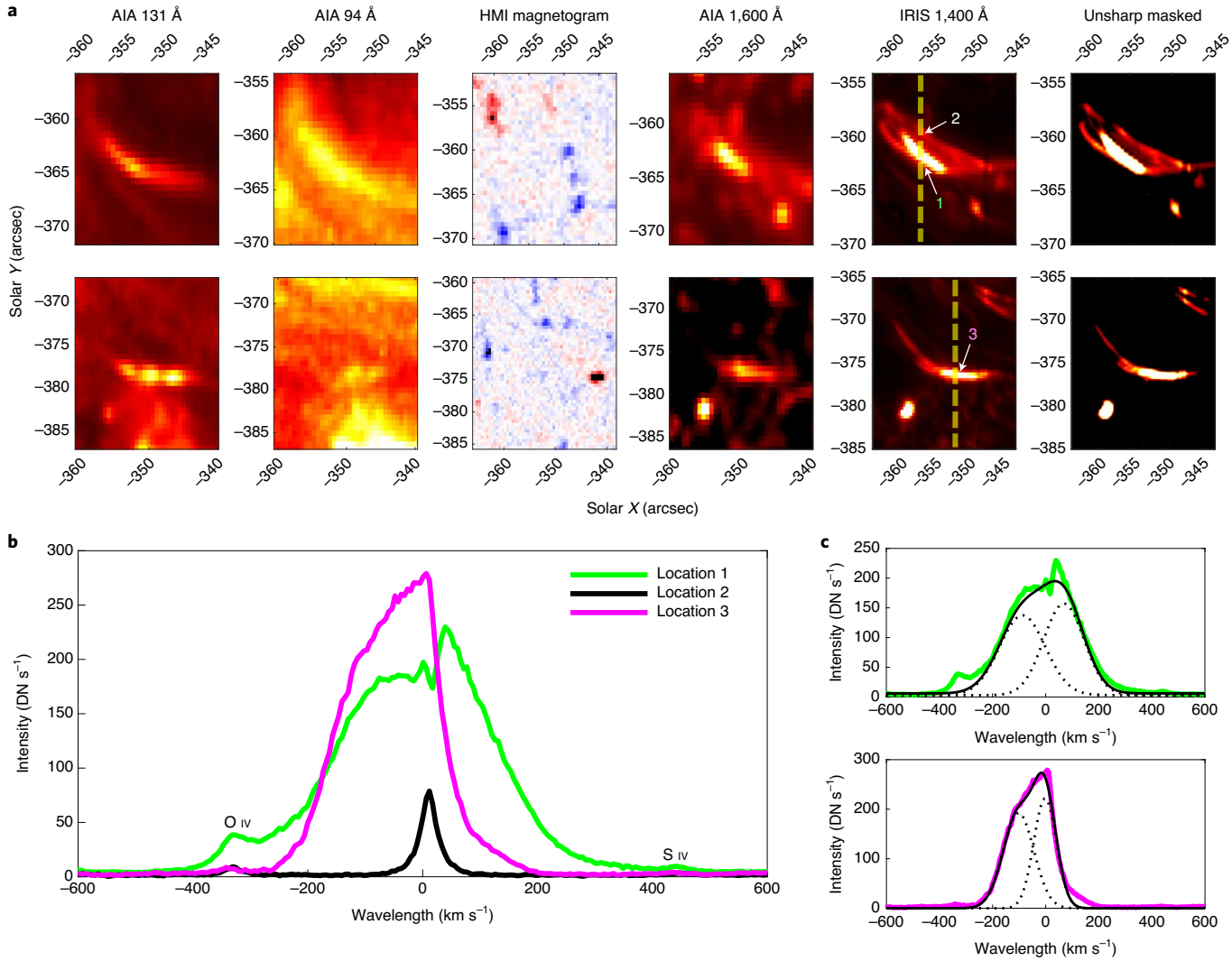


**Fig. 1 | Co-aligned IRIS, SDO/AIA and SDO/HMI images of the observed loop brightenings and the associated spectra at the pixel locations of the brightenings. a**, Candidate loop brightenings observed by SDO/AIA, SDO/HMI and IRIS: (from left to right columns): 131 Å SDO/AIA, 94 Å SDO/AIA, SDO/HMI magnetogram, 1,600 Å SDO/AIA, IRIS 1,400 Å and unsharp masked IRIS 1,400 Å. The images in the top row were observed from 15:29:14 UTC to 15:32:53 UTC and the bottom row from 16:08:08 UTC to 16:14:49 UTC. **b**, Spectral information obtained from IRIS slit measurements for three locations: 1 and 3 where maximum brightening appears to be co-spatial with the loop; and 2 where there is no brightening. The O IV and S IV labels indicate the O IV 1,404.157 Å and S IV 1,404.808 Å emission lines, respectively. **c**, The multi-peaked, broadened Si IV 1,403 Å profile is fitted with a bi-component Gaussian (black, solid lines) for the brightening regions at location 1 (top) and location 3 (bottom). The decomposed components are shown by black, dashed lines. DN, digital number.

ratios are observed at the locations of the brightenings, indicating that non-equilibrium ionization physics driven by impulsive heating plays a key part in explaining the properties of the emission lines. To confirm this relationship, we extended our analysis to four more loops (Supplementary Figs. 2–5) and present our results in a set of histograms (Supplementary Fig. 6). Our findings are consistent with the analysis presented above for locations 1 and 3 of Fig. 1.

We note here that non-equilibrium ionization alone cannot explain the Si IV line broadening relative to O IV. Bradshaw and Testa[11] showed that impulsive heating, coupled to non-equilibrium ionization and density-dependent dielectronic recombination, drives longer-lived ions formed at low temperatures into lower-lying, denser regions of the atmosphere, which causes them to emit more strongly (intensity scales as $n^2$) and has the net effect of increasing the ratio of Si IV intensity to O IV intensity. The emission is spread over a wider range of temperatures, but the range extends from the equilibrium formation temperature towards lower temperatures and favours narrower linewidths. Thus, a mechanism that can substantially heat heavier ions preferentially to lighter ions, broadening the Si IV line profile relative to O IV, is required, which is also consistent with impulsive heating (for example by field-line braiding and reconnection) to explain the large Si IV/O IV intensity ratios.

The case for impulsive heating associated with the brightenings is strengthened by temporally correlating the IRIS emission with the hotter extreme-ultraviolet emission[12] observed by AIA. Time-lags between the light curves of extreme-ultraviolet channel pairs sensitive to different temperatures allow one to determine whether the plasma is heating or cooling[13–15]. Figure 4 (top) shows the light curves for loops at locations 1 and 3 in the IRIS 1,400 Å channel and six AIA extreme-ultraviolet channels (131 Å, 171 Å, 193 Å, 211 Å, 335 Å and 94 Å). In both cases, the peak of the IRIS 1,400 Å

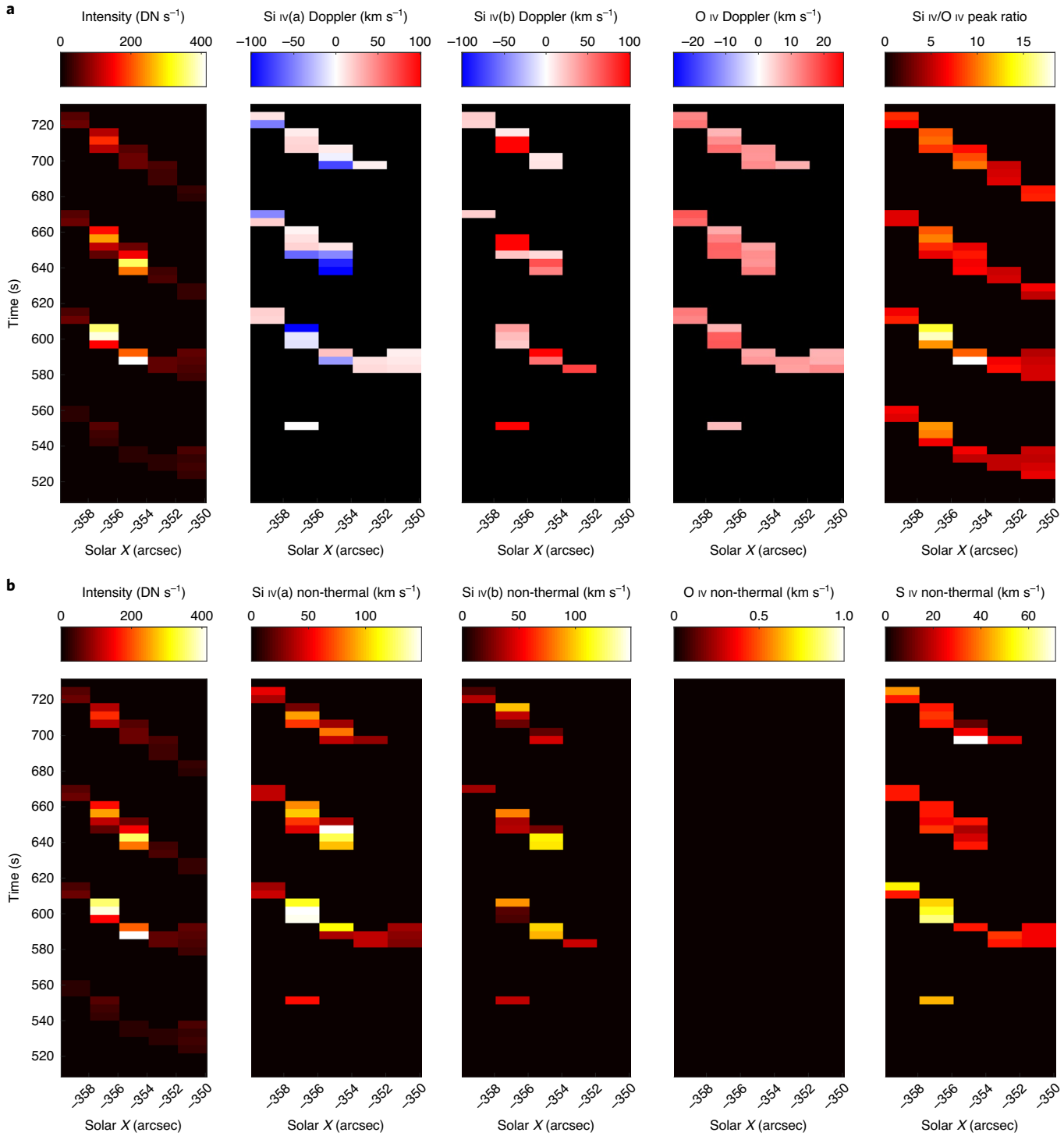


**Fig. 2 | Pixel-by-pixel analysis of the physical parameters along the magnetic loop structure observed at location 1. a**, The temporal evolution (vertical axis) of Si IV intensity, Doppler components extracted from the fitted Si IV lines, Doppler shift from O IV lines, and the peak-to-peak intensity ratio of Si IV to O IV are shown for each pixel (horizontal axis). **b**, The temporal evolution (vertical axis) of intensity and the non-thermal components calculated from the widths of the Si IV, O IV and S IV lines are shown for each pixel.

emission appears at least 20 s earlier than the AIA extreme-ultraviolet emission peaks, providing further evidence that heating events are being observed. The light curves of the AIA extreme-ultraviolet channels peak concurrently, indicating the short timescale of the events.

The properties of the emission measure distribution of the brightening loops yields information regarding timescales on which plasma is re-energized (heating frequency)[7–9,16] and on the presence of 'super-hot' components to the emission[17–19], which are predicted, but hard-to-detect, signatures and evidence of impulsive heating[20,21]. Given that the IRIS and AIA observations demonstrate that the emitting volume along the line-of-sight is not isothermal, the differential emission measure (DEM) provides a more appropriate way to diagnose the heating properties. The two key

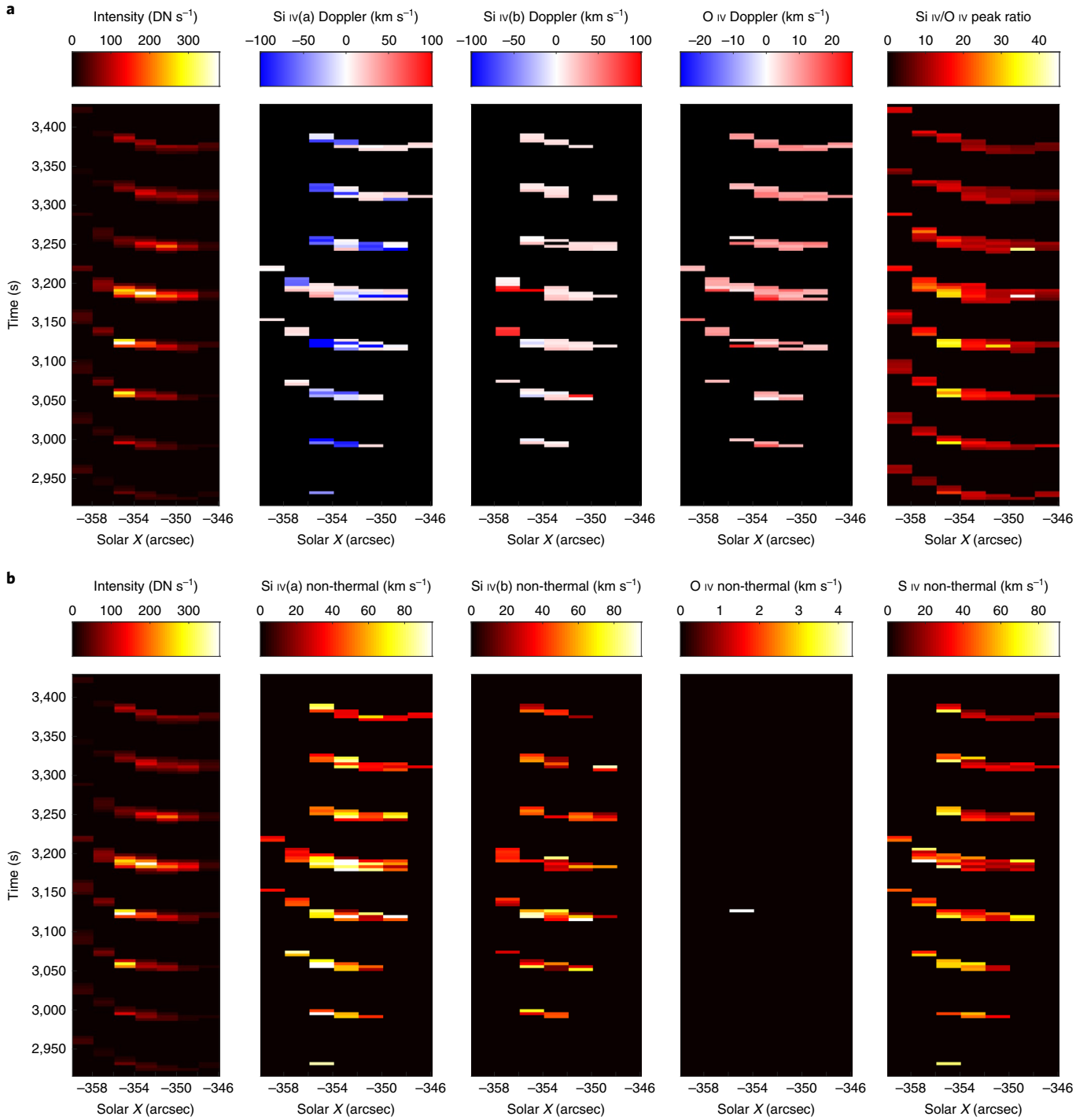


**Fig. 3 | Pixel-by-pixel analysis of the physical parameters along the magnetic loop structure observed at location 3 . a**, The temporal evolution (vertical axis) of Si IV intensity, Doppler components extracted from the fitted Si IV lines, Doppler shift from O IV lines, and the peak-to-peak intensity ratio of Si IV to O IV are shown for each pixel (horizontal axis). **b**, The temporal evolution (vertical axis) of intensity and the non-thermal components calculated from the widths of the Si IV, O IV and S IV lines are shown for each pixel.

properties of the DEM used to diagnose heating are its gradient coolwards of the peak and an enhanced shoulder appearing above the temperature of the peak DEM. The heating frequency is related to the gradient of the DEM, where shallower (steeper) gradients suggest lower (higher) frequency events. An enhanced shoulder to the DEM indicates the presence of hot, but faint and hard-to-detect, emission associated with impulsive heating in loops prior to substantial filling by ablation.

The evolving DEMs at locations 1 and 3 (Fig. 1) are calculated using co-aligned data from the AIA extreme-ultraviolet channels (see Methods) during the brightening events. The middle panel of Fig. 4 shows that the DEMs broaden after the onset of each brightening in the IRIS 1,400 Å channel (location 1 at 600 s and location 3 at 3,000 s), and the gradient coolwards of the peak becomes steeper (gradients $\geq 3$), indicating enhanced heating activity, and at the same time a hot ($T > 10$ MK) shoulder briefly appears, indicating

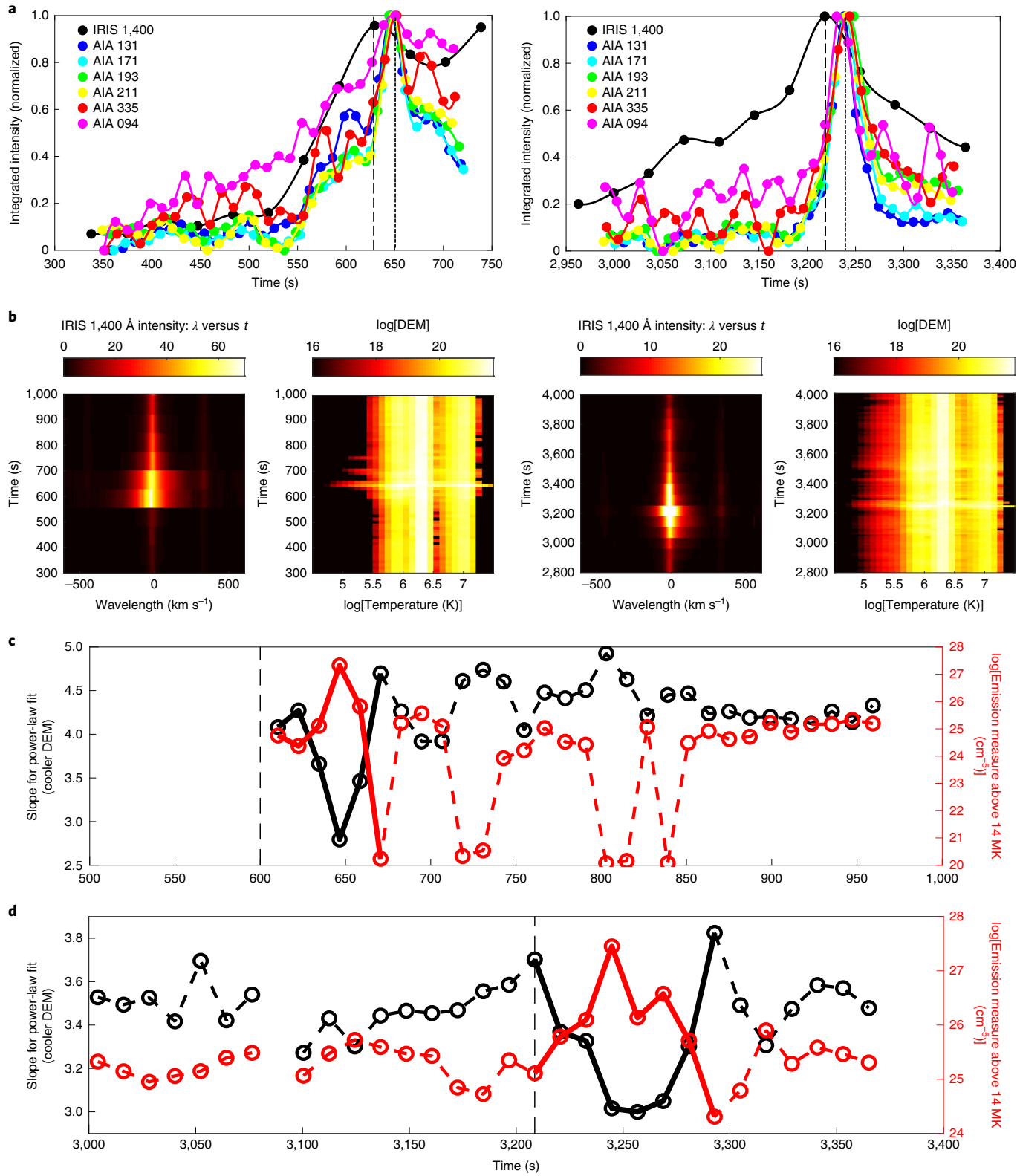


**Fig. 4 | Temporal evolution of the light curves and the DEMs at the locations of loop brightenings. a**, Light curves for the loops at location 1 (left) and location 3 (right) (Fig. 1) are shown for the IRIS 1,400 Å channel (black, solid lines) and six AIA extreme-ultraviolet channels: 131 Å (blue), 171 Å (light blue), 193 Å (green), 211 Å (yellow), 335 Å (red) and 94 Å (magenta). The vertical dashed lines indicate the times when the brightenings first appear in the IRIS 1,400 Å channel and the vertical dotted lines indicate the times when the brightenings first appear in the SDO/AIA channels. **b**, Temporal evolution of the IRIS Si IV spectrum and the DEM distribution obtained from the AIA channels for loops at location 1 (left) and location 3 (right) are shown. **c**,**d**, Temporal evolution of the DEM slope coolwards of the peak (black) and the integrated DEM (logarithmic) above 14 MK for loops (red) at location 1 (**c**) and location 3 (**d**) are presented. Solid lines indicate the lifetimes of the line broadenings at the brightening locations in the IRIS 1,400 Å channel. The vertical dashed lines indicate the times when the brightenings first appear in the IRIS 1,400 Å channel. Uncertainties associated with the measured quantities shown in **a**, **c** and **d** are in the range of 3% of the plotted values but not shown in the figure for the sake of readability.

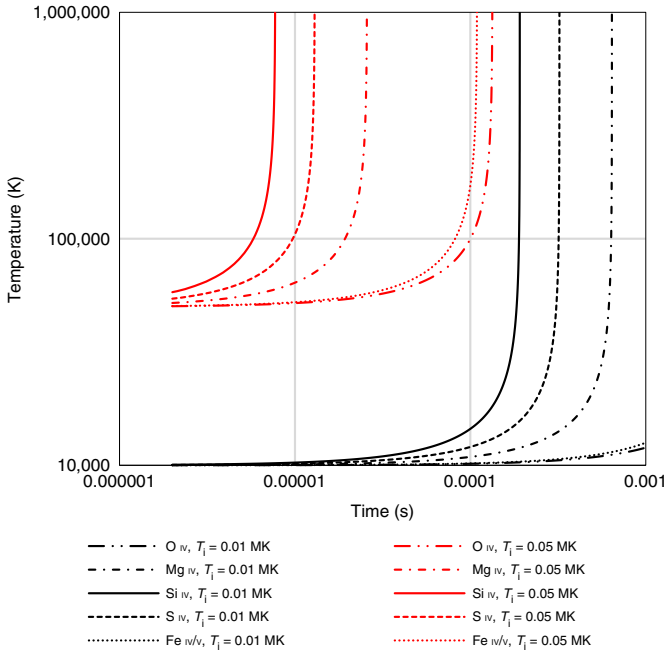


**Fig. 5 | Heating rate due to the ion cyclotron instability for the most abundant heavy species (O, Si, S, Mg and Fe) in the transition region.** Temperature change with respect to time due to the ion cyclotron instability is plotted for different initial temperatures $T_i$. Black lines indicate cooler initial temperature ($T_i = 0.01$ MK), whereas red lines indicate relatively higher temperatures ($T_i = 0.05$ MK) from which the ions are heated. Solid, dashed, dot-dashed, dotted and dot-dot-dashed lines represent the ions of Si IV, S IV, Mg IV, Fe IV and O IV, respectively.

strong impulsive heating. In the lower two panels of Fig. 4 the gradient of the DEMs and the logarithms of the DEMs integrated above 14 MK are given with respect to time. An increase of 2–3 orders of magnitude in the hot part of the emission measure is observed when IRIS sees the event and a sharp decrease in the DEM slope coolwards of the peak is seen. We have computed the temporal evolution of the DEM-weighted temperature at the brightening/heating locations (Extended Data Fig. 2) and found that it transiently exceeds 10 MK at the onset of a brightening, which lends further support to the interpretation of impulsive heating creating hot plasma.

The 20-s time lag between the evolving AIA extreme-ultraviolet light curves, and the DEMs, and the IRIS 1,400 A channel is consistent with timescales in numerical studies of simulated nanoflares where plasma is impulsively heated to multimillion degree temperatures[11]. To conclude our observational analysis, we propose the brief appearance of a hot shoulder to the DEMs is the first detected signature of high-temperature emission due to impulsive heating in non-flaring, low-lying, transition-region loops.

The IRIS image intensity-gradient resolved data coupled with the AIA DEM analysis clearly show that the loop brightenings are associated with heating at the pixel locations where there is a strong concentration of sub-resolution strands. At the same pixels, the IRIS spectroscopic data show bi-directional flows, with strong non-thermal components, in the heavier ion lines (Si IV and S IV), while exhibiting no such features in the lighter ion line (O IV). From this observational evidence, we conjecture that plasma heating and the associated brightenings originate at braiding sites where strong currents exist and magnetic reconnection drives strong outflows, and where ion cyclotron waves leading to turbulence arise. Depending on the ratio of electron temperature to ion temperature, and the ratio of number densities of the different species[22], each ion species in the multi-ion plasma must exceed a critical drift velocity to trigger the ion cyclotron instability and undergo heating by turbulence. We can show in the transition region that silicon and sulfur, in particular, have smaller drift velocities and thus shorter onset times for the instability. Consequently, they experience the strongest heating.

Our reasoning is based on the expectation that the magnetic field is close to force-free in the transition region, and that strong currents and ion cyclotron waves arise at braiding sites, where the length of the current sheet is within the spatial scale of the observed structures (see Methods). Ion cyclotron waves are subject to instabilities that generate magnetic fluctuations that energize and scatter particles in random directions, resulting in electron and ion heating. In the case of ion cyclotron instabilities, the ion heating rate is weakly proportional to $m_{ion}$ (refs. [22–24]) and the critical drift velocity is smaller for the more abundant heavier ions. In Fig. 5 we plot the ion heating rate for the most abundant heavy species (O, Si, S, Mg and Fe) in the transition region, for a temperature range 0.01–0.05 MK, and show that the silicon and sulfur ions gain energy from the magnetic field at a much faster rate than the other species. This result demonstrates that heating by reconnection and ion cyclotron turbulence associated with the sites of magnetic braiding can provide a physical explanation for the observed high-intensity ratios of Si IV/O IV (heating) at the brightening sites associated with bi-directional flows (reconnection) and non-thermal broadening (turbulence).

We have also carefully ruled out several mechanisms that could explain some features of the observations including: thermal non-equilibrium cycles under non-equilibrium ionization conditions (Supplementary Tables 2 and 3), heating and line broadening by magneto-acoustic shocks (Extended Data Fig. 3), and line broadening coupled with self-absorption in the Si IV line due to chromospheric reconnection (Extended Data Figs. 4 and 5). The analysis is extended for the additional four loops as well (Supplementary Figs. 7 to 10). In addition, the sound speed in the transition region (at $T \approx 10^5$ K) is around 45 km s$^{-1}$ and so one may expect that shocks have a role in the heating process. However, the observed bidirectional flow speed peaks at 100 km s$^{-1}$. Under such conditions, even if all of the energy of the flow went into the ions then equating the thermal and kinetic energies yields a temperature increase of $\sim 10^5$ K($\ll 1$ MK), which is not sufficient to explain the observed line broadenings in Si IV and S IV, and cannot account for the lack of O IV line broadening.

## Methods

The IRIS telescope feeds a far-ultraviolet band (from 1,332 Å to 1,407 Å) and a near-ultraviolet band (from 2,783 Å to 2,835 Å) and the light passes through a spectrograph system to record spectral data[1]. The observation of interest is a large, coarse 8-step raster scan of solar active region AR12396. The scan was taken on 2015 August 06 from 15:19:21 to 16:41:59 Coordinated Universal Time (UTC) with a field of view of 14′ × 119′ at the centre location: $x$, $y$: −357″, −369″. The 0.33″ × 119″ slit was stepped 8 times with 2″ steps and a step cadence of 9.1 s. However, this observation consists of the repetition of 68 such frames, making the total raster cadence for each loop 73 s. Thus, the total number of raster scans is 544. The slit-jaw images had a field of view of 120′ × 119′ with a cadence of 36 s. Since the slit-jaw image cadence is four times longer than the raster cadence, there are 136 slit-jaw images in total. All of the data are calibrated to level 2 by including dark current, flat-field and geometric correction, and subsequently transformed to level 3 data by building data cubes of spatially and temporally sequenced spectra.

The selection of suitable loops is based on two criteria: (1) the brightened arc is small enough to be considered a transition-region loop (<10 Mm) and (2) the intensity profile of the pixels is distinguishable above the noise threshold. However, since the raster scans through the entire image, it covers the loop only for a fraction of its evolution. Next, we extract the spectral data from the raster file. To determine line and continuum intensities, we fit each line profile by employing a double-peak Gaussian fitting algorithm with a background baseline. The baseline is first estimated within multiple shifted windows of width 200 separation units and by regressing the varying baseline to the window points, using a spline approximation, we adjust the baseline for the corresponding spectrum. Once the fitted spectrum was retrieved, we extracted the O IV 1,399.766 Å, O IV 1,401.157 Å, Si IV 1,402.77 Å and S IV 1,404.808 Å peaks. Here, the temporal lengths of the loops discussed in

Fig. 1 are 15:29:14 to 15:32:53 for position 1 and 16:08:08 – 16:14:49 for position 3 respectively.

For Fig. 1, each frame of the IRIS slit-jaw image 1,400 Å image is upsampled (bicubic interpolation) by a factor of 5 and sharpened by subtracting a blurred (unsharp) version of the image from itself (MATLAB built-in functions: imresize and imsharpen), similar to in ref. [10]. Since the new image is resized by a factor of 5, the standard deviation of the Gaussian low pass filter for unsharp masking is set to 5 ($\sigma = 5$ pixels). The strength of the sharpening effect for an edge pixel is set to 3. This value can be increased to introduce sharper contrast; however, an excessively large value for this parameter may create undesirable artifacts in the resulting image.

We extract observational parameters of physical importance, namely the peak ratio of the O IV 1,401.157 Å and Si IV 1,402.77 Å lines, and the Doppler shift and linewidth of O IV 1,401.157 Å, Si IV 1,402.77 Å, and S IV 1,404.808 Å lines. The Si IV 1,402.77 Å line did not exhibit a single Gaussian or Lorentzian form, so we adopted a bi-component Gaussian (since it fitted with minimum root-mean-squared error, which was always less than 3%) for this line and then measured the width and Doppler shift for each component. From the linewidth of the measured lines, we calculated the non-thermal broadening with the equation

$$\Delta v_{\text{non-th}} = \sqrt{\Delta v^2 - \Delta v_{\text{th}}^2 - \Delta v_{\text{inst}}}$$

where $\Delta v_{\text{th}}$ is the maximum thermal line broadening at the peak formation temperature in the transition region. We note that a reliable component analysis could not be done for S IV bulk flow owing to its weak signal strength and the presence of blending lines from O IV 1,404.779 Å; thus, a single-component analysis is performed and shown in Extended Data Fig. 1.

We employ the atomic database Chianti[25] to calculate the theoretical intensity ratio of pairs of 1,400 Å lines from the O IV ion as a function of density. We then interpolate our observation with this theoretical model and derive the density for each pixel, at each time step (Supplementary Information).

We have aligned the IRIS data to the AIA 1,600 Å channel and the AIA 1,600 Å channel to the other extreme-ultraviolet channels using the solar limb (Extended Data Fig. 6). Since our spatial scales are extremely small, we revise the co-alignments by trial and error and exclude any unrelated bright pixel in the region of interest. Finally, we isolated the pixel coordinates from the IRIS slit-jaw image observed in the 1,400 Å channel and the corresponding AIA extreme-ultraviolet channels and integrated the pixel intensities to obtain the light curves.

We found that the peak of the IRIS 1,400 Å emission appears at least 20 s earlier than the AIA extreme-ultraviolet emission peaks. Although this timescale supports numerical studies from the literature[11], we present a back-of-the-envelope calculation to demonstrate its consistency: assuming a loop of 10 Mm ($10^9$ cm) in length and $10^{14}$ cm$^2$ (width of strand below spatial resolution) in cross-section yields a volume of $V = 10^{23}$ cm$^3$; if the density $n = 10^{11}$ cm$^{-3}$ and the (initially low) plasma temperature increases by $dT = 5$ MK then the timescale $\tau$ is given, roughly, by $3\frac{k_B n dT}{\tau} = H$. Setting $H = 10$ erg cm$^{-3}$ s$^{-1}$ gives an energy input of $H \times V = 10^{24}$ erg s$^{-1}$ and $\tau = 20$ s. The total energy input is then $H \times V \times \tau = 2 \times 10^{25}$ erg, which is more powerful than the canonical nanoflare but still much weaker than a microflare, for example, for a set of very reasonable parameter values. Here, we have also assumed that energy redistribution by thermal conduction is, initially, relatively inefficient in the dense plasma, and radiative losses are small as the plasma reaches high temperatures quite quickly.

For the calculation of the DEM for each pixel, shown in Fig. 4, we adopted the regularized inversion technique of Hannah and Kontar[26]. An IDL routine can be found in GitHub to efficiently implement this technique: https://github.com/ianan/demreg.

It is difficult to know for certain whether the magnetic field is force-free in the transition region observed by IRIS, or whether it is a better assumption in some parts of the Sun than in others (for example, quiet Sun versus active regions). Although currents are needed to drive ion cyclotron waves, they need not be strictly field-aligned and so the field need not be exactly force-free. In addition, we point to the study conducted by Metcalf et al.[27]. where the magnetic field in NOAA active region 7216 was measured and it was concluded that the field becomes force-free at a location in the chromosphere about 400 km above the photosphere, which is significantly below the heights we are considering.

Assuming a nearly force-free field, strong field-aligned currents at braiding sites in transition region loops could drive ion cyclotron waves at those locations. We can calculate the length of the current sheet for the structures of interest to us using the set of expressions for the Spitzer values[28]

$\eta = \frac{1}{3} L^2/\tau$ where $L$ is the length of the current sheet and $\tau$ is the heating timescale

$\eta = 65.8 T_e^{\frac{3}{2}} \ln\Lambda$ where $T_e$ is the electron temperature and In$\Lambda$ is the slowly varying Coulomb logarithm.

In the transition region, $T_e = 10^5$ K, In$\Lambda = 15$ and observationally we found $\tau = 20$ s leading to $L = 1{,}500$ km, which is well within the spatial scale of the magnetic structures we are considering of around $O(10^9)$ cm $\cong$ 10,000 km.

As mentioned in the main text, ion cyclotron waves are subject to instabilities which generate magnetic fluctuations that energize and scatter particles in random directions, resulting in electron and ion heating[22]:

$$\left(\frac{\partial T_e}{\partial t}\right)^* = \frac{2}{3}\frac{m_e}{k_B} v_e^* V_{d,e}^2 \text{ for electrons and} \quad (1)$$

$$\left(\frac{\partial T_i}{\partial t}\right)^* = \frac{2}{3}\frac{m_i}{k_B} v_i^* V_{d,e}^2 \text{ for ions.} \quad (2)$$

Here $v_e^*$, $v_i^*$ are the electron and ion collision frequencies, respectively, and $V_{d,e}$ is the electron drift velocity. The heating can be initiated by the ion acoustic instability or the ion cyclotron instability. In the case of the ion acoustic instability:

$$\left(\frac{\partial T_i}{\partial t}\right)^* \propto \frac{1}{\sqrt{m_i}}$$

Lighter ions (for example O IV) are heated more rapidly than heavier ions (for example Si IV, S IV), resulting in greater excess line broadening in the lighter species, which we did not observe.

Since ion acoustic turbulence is not consistent with the observed O IV and Si IV linewidths, we turn to a detailed examination of the ion cyclotron instability. The first step is to inspect the ratio of heating rates between O IV and Si IV ions initiated by ion cyclotron instability.

One can rewrite the rate of change of the ion temperature using the relationship $n_i m_i v_i^* = n_e m_e v_e^*$:

$$\left(\frac{\partial T_i}{\partial t}\right)^* = \frac{2}{3}\frac{m_e}{k_B}\frac{n_e}{n_i} v_e^* V_{d,e}^2 \quad (3)$$

The threshold criterion for the instability is (according to ref. [22]):

$$V_{d,e} > V_c = 15\frac{T_i}{T_e} V_{th,i} \quad (4)$$

At marginal stability:

$$V_{d,e} = V_c \quad (5)$$

The anomalous collision frequency is given by:

$$v_e^* = \alpha \Omega_i \left(\frac{V_{d,e}}{V_c} - 1\right)^2 \quad (6)$$

where $\Omega_i$ is the cyclotron frequency in radians per second (cgs units):

$$\Omega_i = \frac{qB}{m_i c} \quad (7)$$

Clearly, we cannot evaluate equation (6) at marginal stability ($V_{d,e} = V_c$), since $v_e^* = 0$.

Therefore, we express $V_{d,e}$ in multiples $N$ of $V_c$, where $N > 1$:

$$V_{d,e} = N V_c \quad (8)$$

Thus:

$$v_e^* = \alpha \frac{qB}{m_i c}(N-1)^2 \quad (9)$$

Substituting equations (8) and (9) into equation (3):

$$\left(\frac{\partial T_i}{\partial t}\right)^* = \frac{2}{3}\frac{m_e}{k_B}\frac{n_e}{n_i}\alpha\frac{qB}{m_i c}(N-1)^2 N^2 V_c^2$$

$$\left(\frac{\partial T_i}{\partial t}\right)^* = \frac{150 m_e}{k_B c}\frac{\alpha q B}{m_i}\frac{n_e}{n_i}\left(\frac{T_i}{T_e}\right)^2 (N-1)^2 N^2 V_{th,i}^2$$

$$\left(\frac{\partial T_i}{\partial t}\right)^* = \frac{150 m_e}{k_B c}\frac{\alpha q B}{m_i}\frac{n_e}{n_i}\left(\frac{T_i}{T_e}\right)^2 (N-1)^2 N^2 \frac{k_B T_i}{m_i}$$

$$\left(\frac{\partial T_i}{\partial t}\right)^* = \frac{150}{c}\alpha q B \frac{T_i^3}{T_e^2}\frac{m_e}{m_i^2}\frac{n_e}{n_i}(N-1)^2 N^2 \quad (10)$$

Taking the limit $N >> 1$:

$$\left(\frac{\partial T_i}{\partial t}\right)^* = \frac{150 N^4 \alpha q B}{c}\frac{T_i^3}{T_e^2}\frac{m_e}{m_i^2}\frac{n_e}{n_i} \quad (11)$$

For a given pair of ions, the rate of (non-thermal) heating will depend on the relative magnitude for each ion of the quantity:

$$f_i = \frac{q_i T_i^3}{m_i^2 n_i} \text{ where } n_i = Y_i \text{Ab} n_H$$

Here, $Y$ is the ion population fraction, Ab is the element abundance relative to hydrogen and $n_H$ is the number density of hydrogen.

Since O IV and Si IV have the same charge, we have $q_{O\,IV}=q_{Si\,IV}$:

$$T_{O\,IV} \approx 1.58\times 10^5\ \mathrm{K}\times T_{Si\,IV} \approx 8\times 10^4\ \mathrm{K}$$

$$m_{O\,IV} = 2.66\times 10^{-23}\ \mathrm{g}\times\ m_{Si\,IV} \approx 4.66\times 10^{-23}\ \mathrm{g}$$

Using the abundance set from Asplund[29] and Chianti ionization data[25]:

$$\mathrm{Ab(O)} = \frac{10^{8.64}}{10^{12}} = 4.9\times 10^{-4},\ \mathrm{Ab(Si)} = \frac{10^{7.51}}{10^{12}} = 3.24\times 10^{-5}$$

$$Y_{O\,IV}(T_i) = 0.67,\ Y_{Si\,IV}(T_i) = 0.19$$

$$n_{O\,IV} = 0.67\times 4.9\times 10^{-4} n_H = 3.3\times 10^{-4} n_H,$$

$$n_{Si\,IV} = 0.19\times 3.24\times 10^{-5} n_H = 6.2\times 10^{-6} n_H$$

Now the ratio becomes:

$$\begin{aligned}\frac{f_{Si\,IV}}{f_{O\,IV}} &= \frac{q_{Si\,IV}T_{Si\,IV}^3}{m_{Si\,IV}^2 n_{Si\,IV}}\cdot\frac{m_{O\,IV}^2 n_{O\,IV}}{q_{O\,IV}T_{O\,IV}^3}\\ &= \frac{T_{Si\,IV}^3}{T_{O\,IV}^3}\frac{m_{O\,IV}^2}{m_{Si\,IV}^2}\frac{n_{O\,IV}}{n_{Si\,IV}}\\ &= \frac{(8\times 10^4)^3}{(1.56\times 10^5)^3}\frac{(2.66\times 10^{-23})^2}{(4.66\times 10^{-23})^2}\frac{3.3\times 10^{-4}}{6.2\times 10^{-6}} = 2.25\end{aligned}$$

This means that quantitatively Si IV should be heated faster than O IV. Next, we calculate the magnitudes of the species heating rates due to ion cyclotron turbulence:

$$\left(\frac{\partial T_e}{\partial t}\right)^* = \frac{150N^4\alpha q B}{c}\frac{T_i^3}{T_e^2}\frac{m_e}{m_i^2}$$

Let the efficiency of the anomalous collision processes $\alpha=10^{-3}$ (ref. [22]) (since $\alpha$ is same for all interactions, the relative rates of temperature change between the ions remains the same. Consequently, the conclusion is independent of $\alpha$) and $q=1, B=100\,\mathrm{G}, \frac{T_i^3}{T_e^2}\approx 10^5 K, \frac{m_e}{m_i^2} = \frac{9.11\times 10^{-28}}{(1.67\times 10^{-24})^2} = 3.27\times 10^{20}$with the assumption that the dominant electron–ion interaction is between $e^-$ and $H^+$:

$$\left(\frac{\partial T_e}{\partial t}\right)^* = (7.85\times 10^6)N^4$$

$$\left(\frac{\partial T_i}{\partial t}\right)^* = \left(\frac{T_i}{T_H}\right)^3\left(\frac{m_H}{m_i}\right)^2\frac{n_e}{n_i}\left(\frac{\partial T_e}{\partial t}\right)^*$$

Let the ion and hydrogen temperatures be the same initially. Let most of the electrons be due to hydrogen ionization. $T_i\approx T_H, n_e\approx n_H$:

$$\left(\frac{\partial T_i}{\partial t}\right)^* = \left(\frac{m_H}{m_i}\right)^2\frac{n_H}{Y\times \mathrm{Ab}\times n_H}\left(\frac{\partial T_e}{\partial t}\right)^*$$

$$\left(\frac{\partial T_i}{\partial t}\right)^* = \left(\frac{m_H}{m_i}\right)^2\frac{q_i}{Y\times \mathrm{Ab}}\left(\frac{\partial T_e}{\partial t}\right)^*$$

$$m_{O\,IV} = 2.66\times 10^{-22}\mathrm{g},\ q_{O\,IV} = 3$$

$$Y_{O\,IV} = 0.67\mathrm{Ab(O)} = 4.9\times 10^{-4}$$

$$\left(\frac{\partial T_i}{\partial t}\right)^*_{O\,IV} = \left(\frac{1.67\times 10^{-24}}{2.65\times 10^{-23}}\right)^2\frac{4}{0.67\times 4.9\times 10^{-4}}\left(\frac{\partial T_e}{\partial t}\right)^* = 48\left(\frac{\partial T_e}{\partial t}\right)^*$$

$$m_{Si\,IV} = 4.66\times 10^{-23}\ \mathrm{g},\ q_{Si\,IV} = 3$$

$$Y_{Si\,IV} = 0.19\ \mathrm{Ab(Si)} = 3.24\times 10^{-5}$$

$$\left(\frac{\partial T_i}{\partial t}\right)^*_{Si\,IV} = \left(\frac{1.67\times 10^{-24}}{4.66\times 10^{-23}}\right)^2\frac{4}{0.19\times 3.24\times 10^{-5}}\left(\frac{\partial T_e}{\partial t}\right)^* = 836\left(\frac{\partial T_e}{\partial t}\right)^*$$

Dropping the previous assumption that $T_i$ is at the equilibrium formation temperature of the line ($T_i=T_e$) and, instead, allowing the ion temperatures to be initially similar, we find that Si IV is heated at a rate greater than O IV by a factor $\frac{836}{48}\approx 17$. This can clearly account for the broader Si IV linewidths.

The next step is to calculate the timescales of electron and ion heating by the ion cyclotron instability for different species. By integrating equations (1) and (2) and making substitutions from the expression of $\tau_{T_e}$:

$$\tau_{T_e} \approx \frac{c}{150(N-1)^2N^2\alpha\beta q_e}\frac{T_e^3 m_i^2}{T_i^3 m_e}$$

$$\tau_{T_i} \approx \tau_{T_e}\frac{T_H^3}{T_e T_i^2}\frac{m_i^2}{m_H^2}\frac{n_i}{n_e}\frac{q_e}{q_i}$$

Let $B=100\,\mathrm{G},\ T_e=10^5\,\mathrm{K}$ (close to the formation temperature of O IV and Si IV), and $T_{i=H}=10^4\,\mathrm{K}$. We list the heating timescales below:

$$\tau_{T_e}(N=2, \text{close to threshold}) = 3\,\mathrm{s}$$

$$\tau_{T_e}(N=10, \text{far from threshold}) = 4.05\times 10^{-6}\,\mathrm{s}$$

And, for ions

$$\tau_{T_{O\,IV}}(N=2, \text{close to threshold}) = 6.1\times 10^{-3}\,\mathrm{s}$$

$$\tau_{T_{Si\,IV}}(N=2, \text{close to threshold}) = 3.6\times 10^{-4}\,\mathrm{s}$$

Further away ($N=10$, far from threshold)

$$\tau_{T_{O\,IV}} = 9\times 10^{-6}\,\mathrm{s}$$

$$\tau_{T_{Si\,IV}} = 5.4\times 10^{-7}\,\mathrm{s}$$

Hence, even close to the threshold, the timescale for the ion cyclotron instability for Si IV can be much less than 1 s and it is reasonable to suppose that the energy may be transferred to Si IV very rapidly before O IV (or the electrons) can be energized, leading to the line broadening of Si IV as observed.

Finally, the threshold condition for the ion cyclotron instability is:

$$V_{cc} = 15\frac{T_i}{T_e}V_{th,i}$$

And for the ion acoustic instability it is:

$$V_{ca} = \frac{T_i}{T_e}V_{th,e}$$

Therefore: $\frac{V_{cc}}{V_{ca}} = \frac{15V_{th,i}}{15V_{th,e}} = \frac{15\sqrt{\frac{k_B T_i}{m_i}}}{\sqrt{\frac{k_B T_e}{m_e}}} = 15\sqrt{\frac{T_i m_e}{T_e m_i}}$

Consequently, $\frac{V_{cc}}{V_{ca}}<1$ and the threshold condition for the ion cyclotron instability would be met first. So, a plausible scenario would be that at braiding sites, the favoured ions (in this case Si and S) are heated strongly first (and the other ions and electrons weakly heated) by ion cyclotron turbulence and then the ion acoustic threshold is reached, which triggers further heating of lighter species if possible. We also expect thermalization and inter-species equilibration via collisions.

## Data availability

The observational data used for this study are designated as AR12396 tracking OBS 3860109180 (2015-08-06 15:19:21-16:41:59) and are publicly available for download from the Lockheed Martin Solar and Astrophysics Laboratory at https://iris.lmsal.com/search/. The co-aligned SDO data are also available at the above-mentioned web source. All data that support the findings of this study are available on reasonable request from the corresponding author.

## Code availability

Details of the algorithms used to create the main figures, especially the unsharp masking and the calculation of ion cyclotron instability, is available in the Methods. The codes required to reproduce the results of these algorithms are available on reasonable request from the corresponding author. For the calculation of the DEM, an IDL routine written by Hannah and Kontar[26] is implemented and can be found at https://github.com/ianan/demreg.

Received: 18 May 2020; Accepted: 23 October 2020;
Published online: 7 December 2020

## References

1. De Pontieu, B. et al. The Interface Region Imaging Spectrograph (IRIS). *Sol. Phys.* **289**, 2733–2779 (2014).
2. Hansteen, V. et al. The unresolved fine structure resolved: IRIS observations of the solar transition region. *Science* **346**, 1255757 (2014).

3. Testa, P. et al. Evidence of nonthermal particles in coronal loops heated impulsively by nanoflares. *Science* **346**, 1255724 (2014).
4. De Pontieu, B. et al. On the prevalence of small-scale twist in the solar chromosphere and transition region. *Science* **346**, 1255732 (2014).
5. Innes, D. E., Guo, L. J., Huang, Y. M. & Bhattacharjee, A. IRIS Si IV line profiles: an indication for the plasmoid instability during small-scale magnetic reconnection on the Sun. *Astrophys. J.* **813**, 86 (2015).
6. De Pontieu, B., McIntosh, S., Martinez-Sykora, J., Peter, H. & Pereira, T. M. D. Why is non-thermal line broadening of spectral lines in the lower transition region of the Sun independent of spatial resolution? *Astrophys. J. Lett.* **799**, L12 (2015).
7. Warren, H. P., Brooks, D. H. & Winebarger, A. R. Constraints on the heating of high-temperature active region loops: observations from Hinode and the Solar Dynamics Observatory. *Astrophys. J.* **734**, 90 (2011).
8. Winebarger, A. R. et al. Defining the 'blind spot' of Hinode EIS and XRT temperature measurements. *Astrophys. J. Lett.* **746**, L17 (2012).
9. Warren, H. P., Winebarger, A. R. & Brooks, D. H. A systematic survey of high-temperature emission in solar active regions. *Astrophys. J.* **759**, 141 (2012).
10. Cirtain, J. W. et al. Energy release in the solar corona from spatially resolved magnetic braids. *Nature* **493**, 501–503 (2013).
11. Bradshaw, S. J. & Testa, P. Quantifying the influence of key physical processes on the formation of emission lines observed by IRIS. I. Non-equilibrium ionization and density-dependent rates. *Astrophys. J.* **872**, 123 (2019).
12. Lemen, J. R. et al. in *The Solar Dynamics Observatory* (eds Chamberlin, P. et al.) 17–40 (Springer, 2011).
13. Viall, N. M. & Klimchuk, J. A. Evidence for widespread cooling in an active region observed with the SDO atmospheric imaging assembly. *Astrophys. J.* **753**, 35 (2012).
14. Lionello, R., Alexander, C. E., Winebarger, A. R., Linker, J. A. & Mikić, Z. Can large time delays observed in light curves of coronal loops be explained in impulsive heating? *Astrophys. J.* **818**, 129 (2016).
15. Viall, N. M. & Klimchuk, J. A. The transition region response to a coronal nanoflare: forward modeling and observations in SDO/AIA. *Astrophys. J.* **799**, 58 (2015).
16. Bradshaw, S. J., Klimchuk, J. A. & Reep, J. W. Diagnosing the time-dependence of active region core heating from the emission measure. I. Low-frequency nanoflares. *Astrophys. J.* **758**, 53 (2012).
17. Barnes, W. T., Cargill, P. J. & Bradshaw, S. J. Inference of heating properties from 'hot' non-flaring plasmas in active region cores. I. Single nanoflares. *Astrophys. J.* **829**, 31 (2016).
18. Cargill, P. J. Active region emission measure distributions and implications for nanoflare heating. *Astrophys. J.* **784**, 49 (2014).
19. Barnes, W. T., Cargill, P. J. & Bradshaw, S. J. Inference of heating properties from 'hot' non-flaring plasmas in active region cores. II. Nanoflare trains. *Astrophys. J.* **833**, 217 (2016).
20. Cargill, P. J. Some implications of the nanoflare concept. *Astrophys. J.* **422**, 381–393 (1994).
21. Cargill, P. J. & Klimchuk, J. A. Nanoflare heating of the corona revisited. *Astrophys. J.* **605**, 911 (2004).
22. Forme, F. R. E., Wahlund, J. E., Opgenoorth, H. J., Persson, M. A. L. & Mishin, E. V. Effects of current driven instabilities on the ion and electron temperatures in the topside ionosphere. *J. Atmos. Terr. Phys.* **55**, 647–666 (1993).
23. Satyanarayana, P., Chaturvedi, P. K., Keskinen, M. J., Huba, J. D. & Ossakow, S. L. Theory of the current-driven ion cyclotron instability in the bottomside ionosphere. *J. Geophys. Res. Space Phys.* **90**, 12209–12218 (1985).
24. Marsch, E., Vocks, C. & Tu, C. Y. On ion-cyclotron-resonance heating of the corona and solar wind. *Nonlin. Process. Geophys.* **10**, 101–112 (2003).
25. Del Zanna, G., Dere, K. P., Young, P. R., Landi, E. & Mason, H. E. CHIANTI – An atomic database for emission lines. Version 8. *Astron. Astrophys.* **582**, A56 (2015).
26. Hannah, I. G. & Kontar, E. P. Differential emission measures from the regularized inversion of Hinode and SDO data. *Astron. Astrophys.* **539**, A146 (2012).
27. Metcalf, T. R., Jiao, L., McClymont, A. N., Canfield, R. C. & Uitenbroek, H. Is the solar chromospheric magnetic field force-free? *Astrophys. J.* **439**, 474–481 (1995).
28. Ashbourn, J. M. A. & Woods, L. C. Energy transport in the solar transition layer. *Proc. Math. Phys. Eng. Sci.* **457**, 1873–1888 (2001).
29. Asplund, M., Grevesse, N., Sauval, A. J. & Scott, P. The chemical composition of the Sun. *Annu. Rev. Astron. Astrophys.* **47**, 481–522 (2009).


## Acknowledgements

This research was supported by the National Aeronautics and Space Administration (grant number NNX15AF97A). We acknowledge the contributions of the LMSAL/IRIS science team and the NASA/SDO including the AIA and HMI science teams for the observational data. IRIS is a NASA Small Explorer Mission developed and operated by LMSAL with mission operations executed at NASA Ames Research Center and major contributions to downlink communications funded by ESA and the Norwegian Space Centre.

## Author contributions

S.M.B. carried out the project as part of research towards the doctoral degree, including data analysis, interpretation and curation, formal analysis, and developing the necessary methodologies and validation schemes. S.J.B. co-conceived the project and is a co-investigator of the funding grant, undertook formal analysis, and supervised this work as part of S.M.B.'s doctoral thesis at Rice University. A.R.W. co-conceived the project and is the principal investigator of the funding grant. The original draft was written by S.M.B., with revisions by S.J.B. and A.R.W.

## Competing interests

The authors declare no competing interests.

## Additional information

**Extended data** is available for this paper at https://doi.org/10.1038/s41550-020-01263-2.

**Supplementary information** is available for this paper at https://doi.org/10.1038/s41550-020-01263-2.

**Correspondence and requests for materials** should be addressed to S.M.B.

**Peer review information** *Nature Astronomy* thanks the anonymous reviewers for their contribution to the peer review of this work.

**Reprints and permissions information** is available at www.nature.com/reprints.

**Publisher's note** Springer Nature remains neutral with regard to jurisdictional claims in published maps and institutional affiliations.

© The Author(s), under exclusive licence to Springer Nature Limited 2020

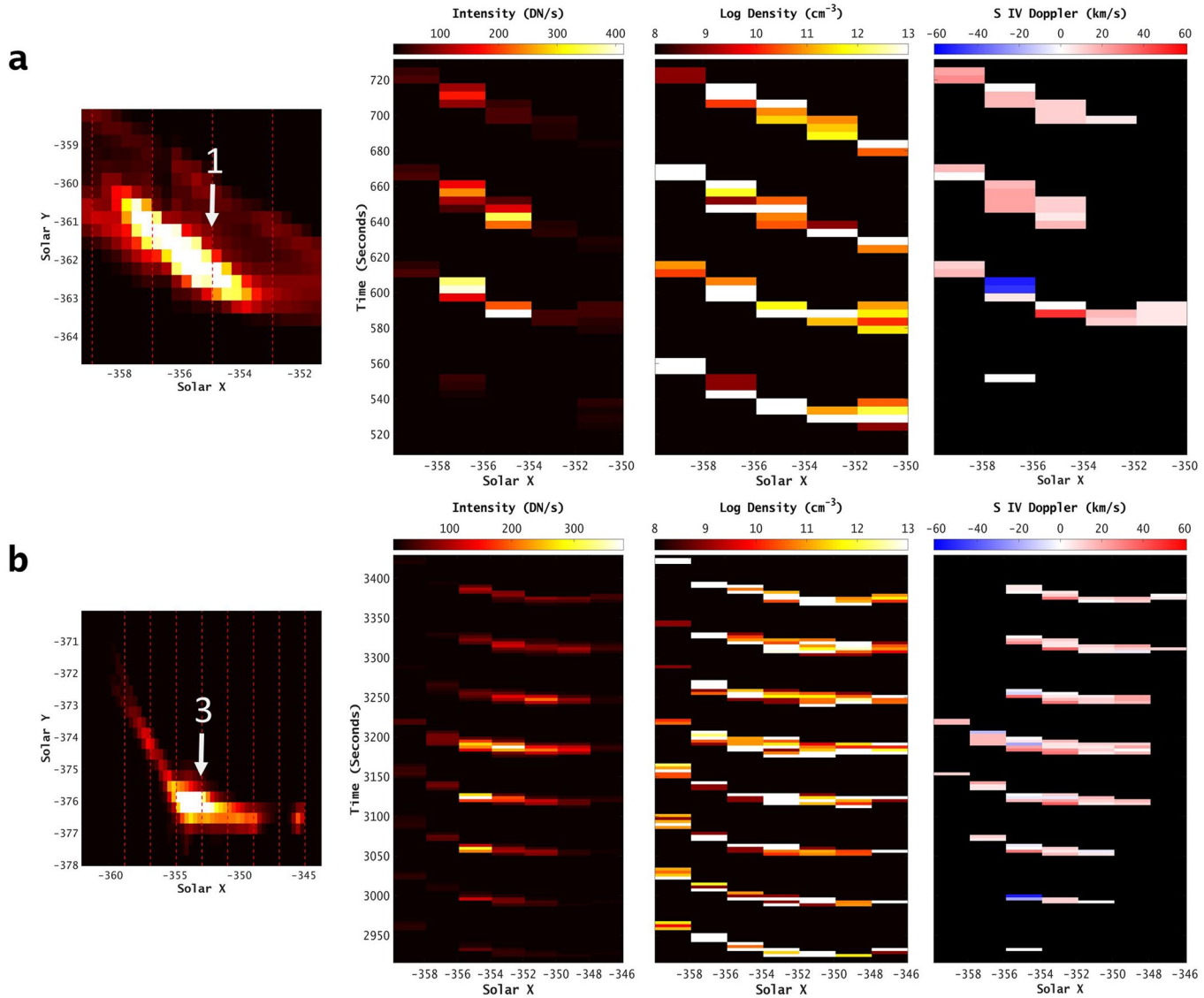


**Extended Data Fig. 1 | Number density and Sulfur IV Doppler evolution of the candidate loop brightenings seen in the IRIS 1,400 Å channel. a**, **b**, (Left to Right) IRIS spectrograph slit positions co-spatial with the loop brightening examined at location 1 (**a**, top row) and location 3 (**b**, bottom row) of Fig. 1; spatiotemporal evolution of intensity, number density, and the single component S IV Doppler velocity is calculated at each slit position.

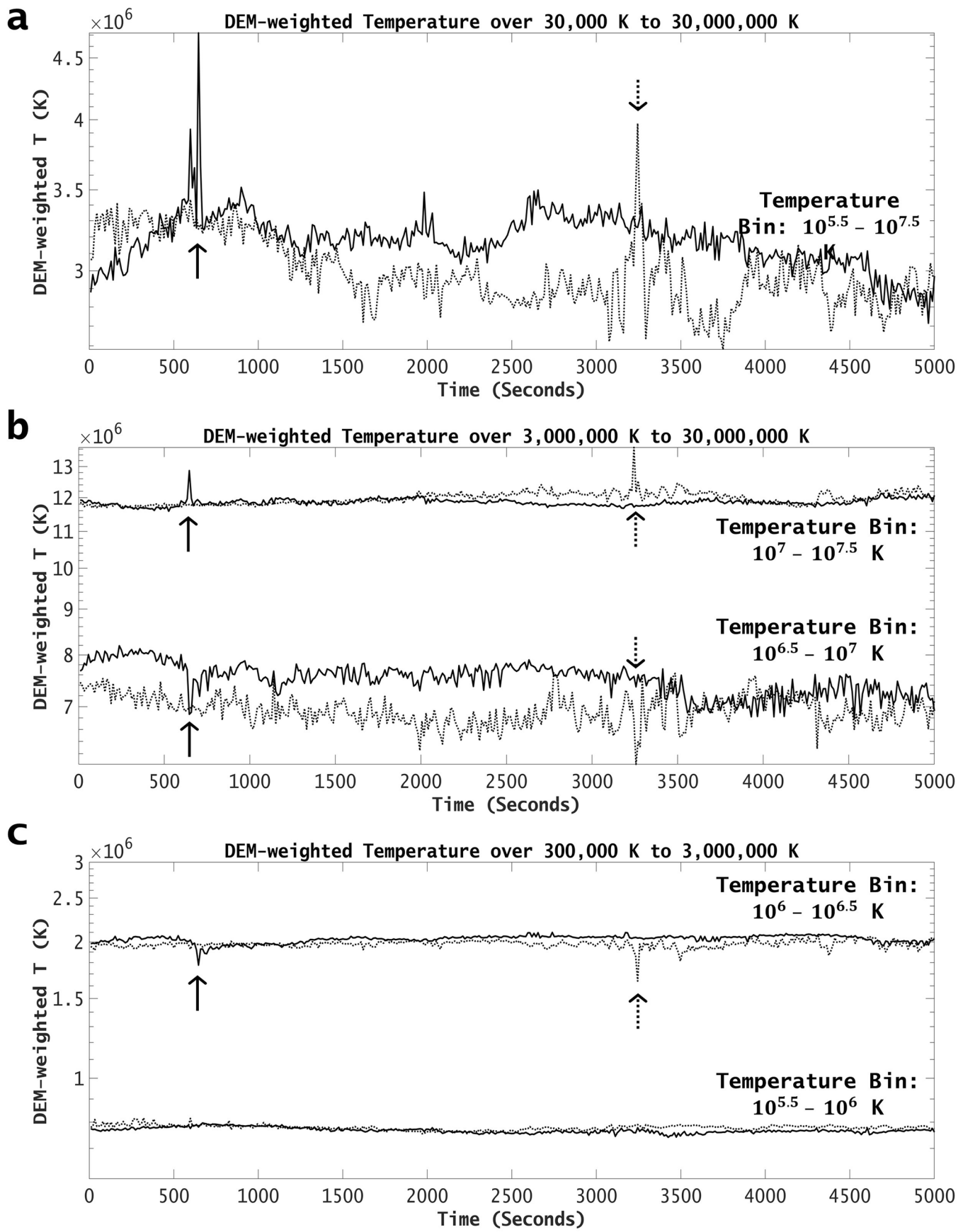


**Extended Data Fig. 2 | See next page for caption.**

**Extended Data Fig. 2 | DEM-weighted temperature *T* for the candidate loops. a**, DEM-weighted temperature *T* for the candidate loops at location 1 (solid) and location 3 (dotted) shown in Fig. 1. **b**, *T* for narrower and hot temperature ranges: $10^{7}$-$10^{7.5}$K and $10^{6.5}$-$10^{7}$K. **c**, ***T*** for cooler temperature ranges: $10^{6}$–$10^{6.5}$K and $10^{5.5}$–$10^{6}$ K. The onset times of impulsive heating events and their associated brightenings are shown by vertical arrows.

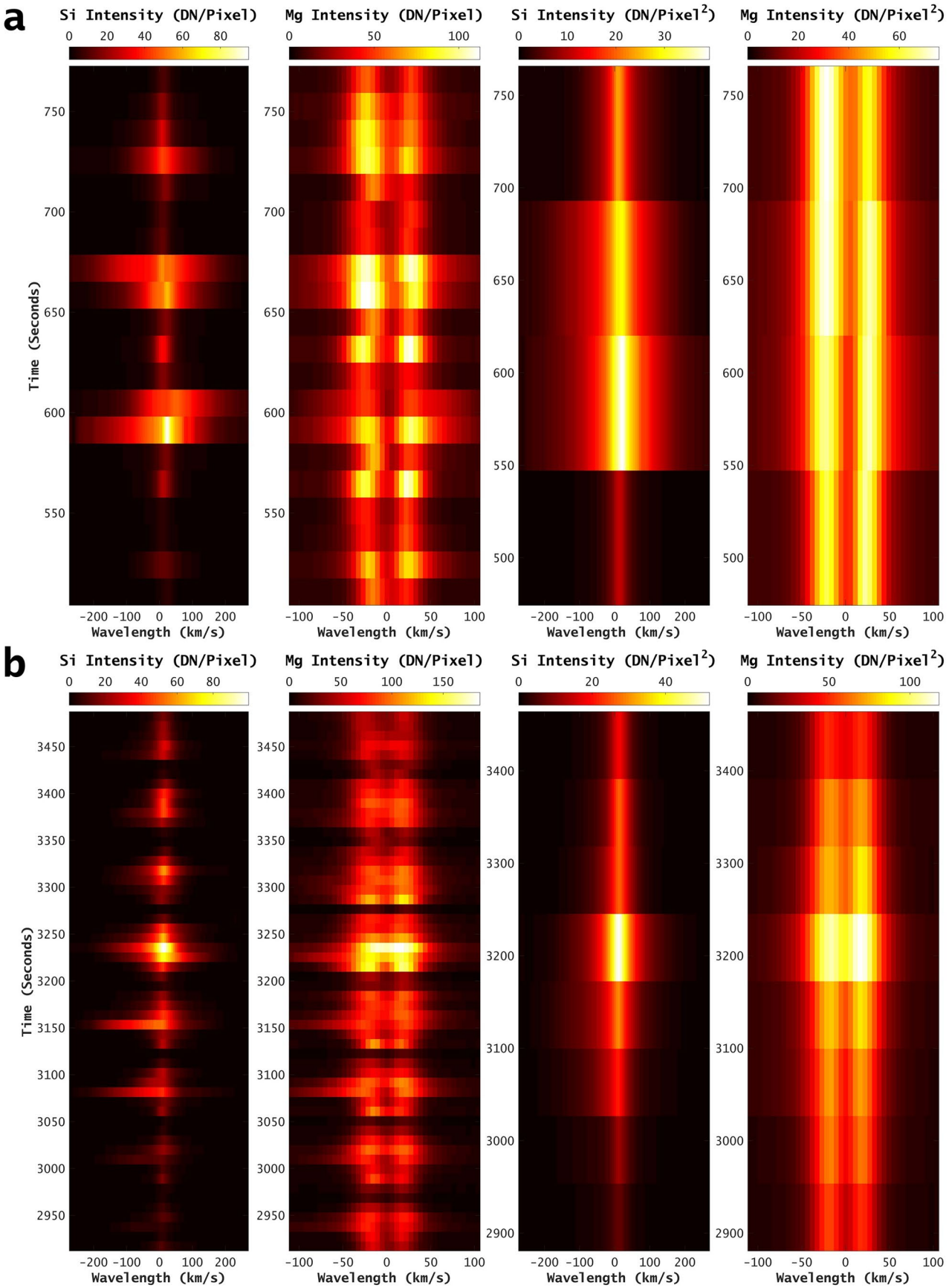


**Extended Data Fig. 3 | See next page for caption.**

**Extended Data Fig. 3 | $\lambda$-$t$ Diagram of candidate loops.** $\lambda$-$t$ diagram of loop brightenings observed at location 1 (**a**) and location 3 (**b**) from Fig. 1. Left to right: temporal evolution of IRIS Si IV and Mg IV spectra where intensity is integrated along the x–axis of the IRIS image; temporal evolution of IRIS Si IV and Mg IV spectra where intensity is integrated along both the x and y axes of the IRIS image. In all cases, the integrated intensity is normalized by the pixel array.

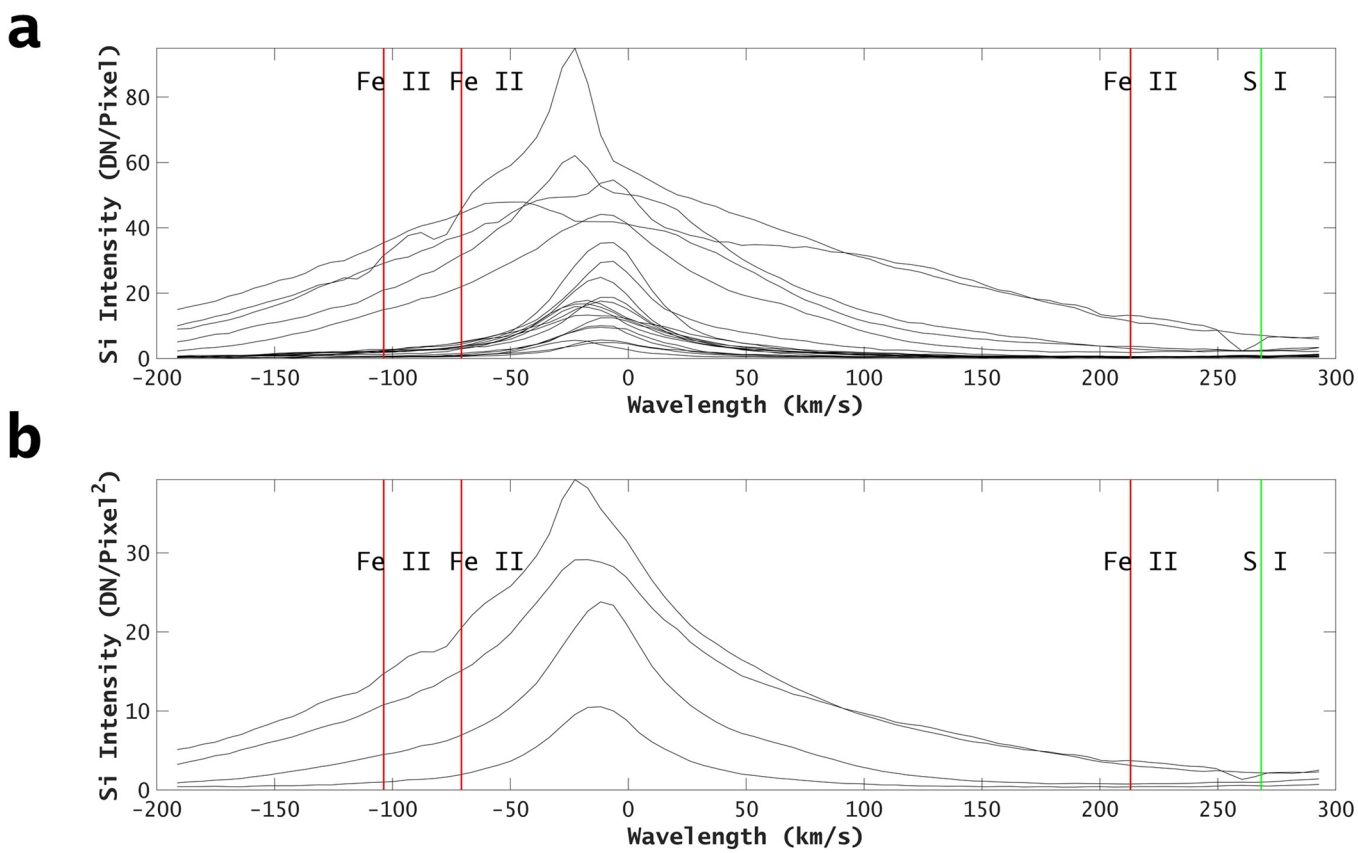


**Extended Data Fig. 4 | Absence of self-absorption lines in candidate loop at location 1. a**, Single pixel array spectra (averaged over y axis) and **b**, spatially averaged (over x-y area) spectra of candidate loop at location 1 in search of self-absorption lines due to chromospheric reconnection-mediated line broadening. Vertical lines indicate possible self-absorption lines present in this channel such as S I 1,401.515 Å (green) and Fe II 1,401.774 Å, 1,403.101 Å, 1,403.255 Å (red).

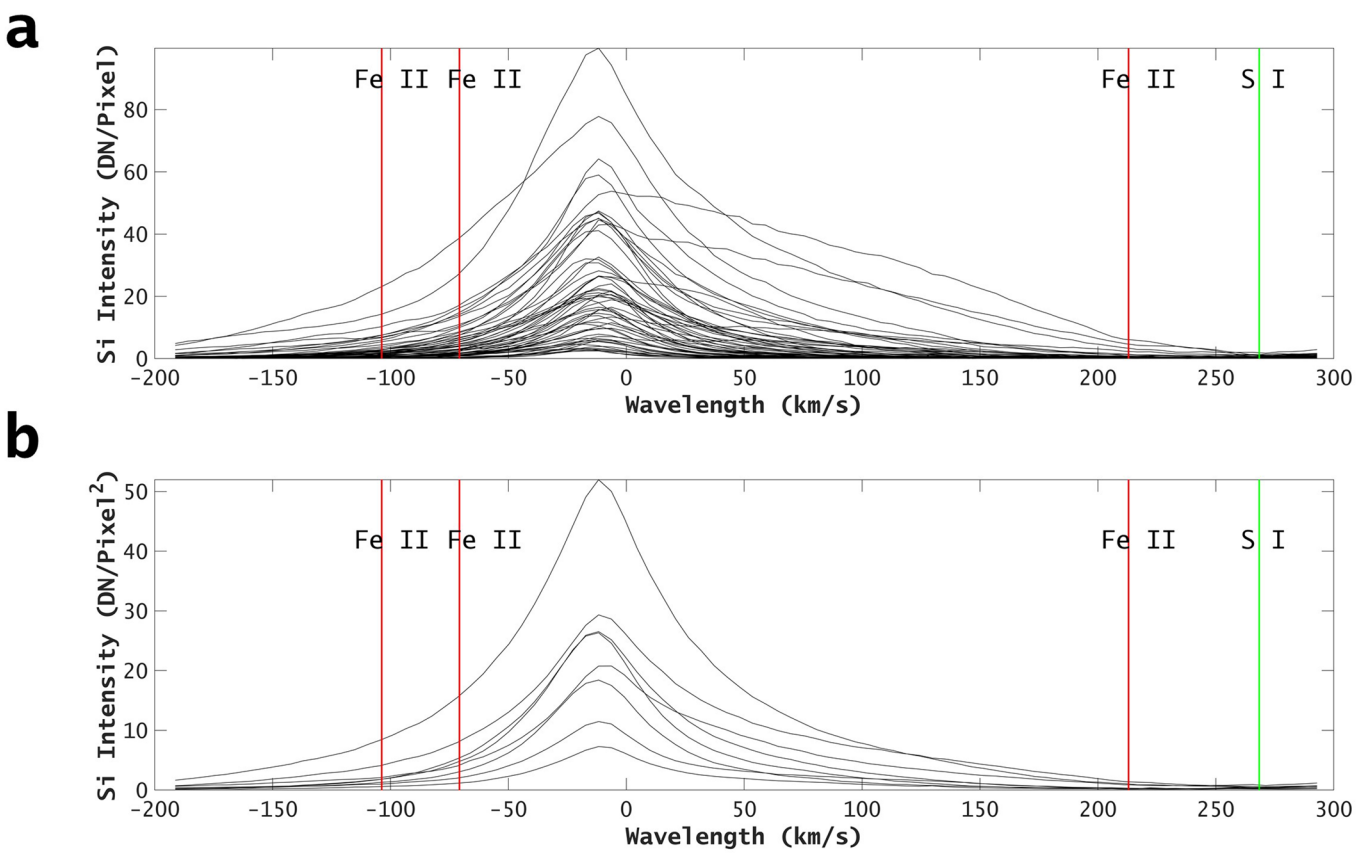


**Extended Data Fig. 5 | Absence of self-absorption lines in candidate loop at location 3. a**, Single pixel array spectra (averaged over y axis) and **b**, spatially averaged (over x–y area) spectra of candidate loop at location 3 in search of possible self-absorption lines. S I 1,401.515 Å (green) and Fe II 1,401.774 Å, 1,403.101 Å, 1,403.255 Å (red) indicated by vertical lines.

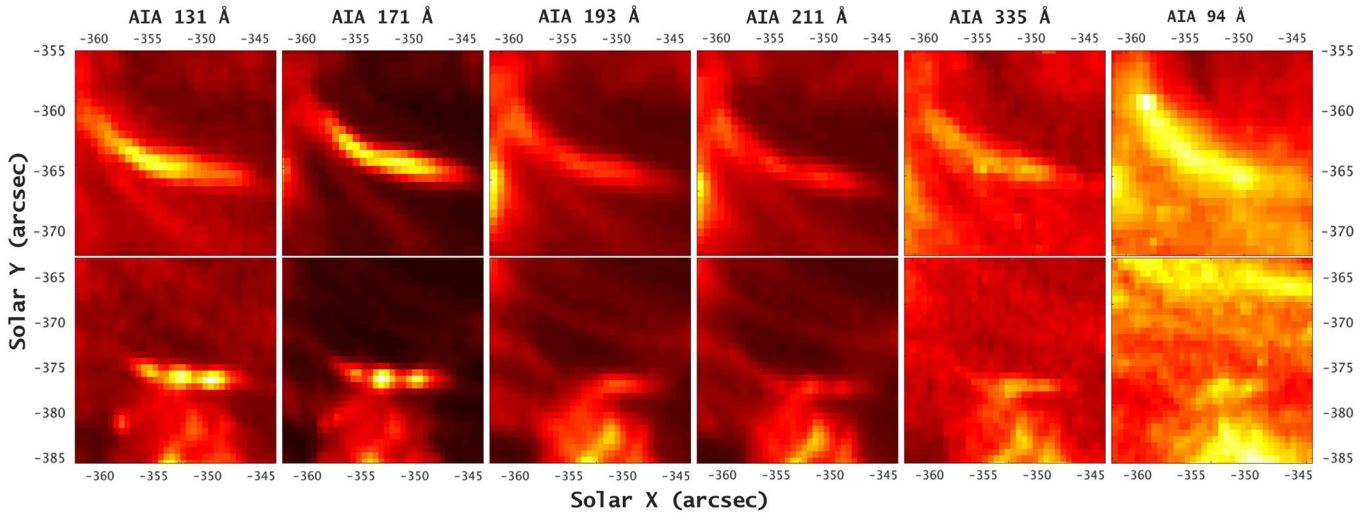


**Extended Data Fig. 6 | Candidate loop brightenings observed in SDO/AIA channels.** Left to right: candidate loop brightenings at location 1 (top) and location 3 (bottom) discussed in Fig. 1 observed in 6 SDO/AIA channels: 131 Å, 171 Å, 193 Å, 211 Å, 335 Å and 94 Å, respectively.